ACS APPLIED MATERIALS & INTERFACES

www.acsami.org Research Article

Controlling Metal–Insulator Transitions in Vanadium Oxide Thin Films by Modifying Oxygen Stoichiometry

Min-Han Lee,* Yoav Kalcheim, Javier del Valle, and Ivan K. Schuller

Cite This: *ACS Appl. Mater. Interfaces* 2021, 13, 887–896 Read Online

ACCESS | Metrics & More | Article Recommendations

Downloaded via UNIV OF CALIFORNIA SAN DIEGO on October 6, 2021 at 05:01:43 (UTC).
See https://pubs.acs.org/sharingguidelines for options on how to legitimately share published articles.

ABSTRACT: Vanadium oxides are strongly correlated materials which display metal–insulator transitions (MITs) as well as various structural and magnetic properties that depend heavily on oxygen stoichiometry. Therefore, it is crucial to precisely control oxygen stoichiometry in these materials, especially in thin films. This work demonstrates a high-vacuum gas evolution technique which allows for the modification of oxygen concentrations in VO_X thin films by carefully tuning the thermodynamic conditions. We were able to control the evolution between VO_2, V_3O_5, and V_2O_3 phases on sapphire substrates, overcoming the narrow phase stability of adjacent Magnéli phases. A variety of annealing routes were found to achieve the desired phases and eventually control the MIT. The pronounced MIT of the transformed films along with the detailed structural investigations based on X-ray diffraction measurements and X-ray photoelectron spectroscopy show that optimal stoichiometry is obtained and stabilized. Using this technique, we find that the thin-film V–O phase diagram differs from that of the bulk material because of strain and finite size effects. Our study demonstrates new pathways to strategically tune the oxygen stoichiometry in complex oxides and provides a road map for understanding the phase stability of VO_X thin films.

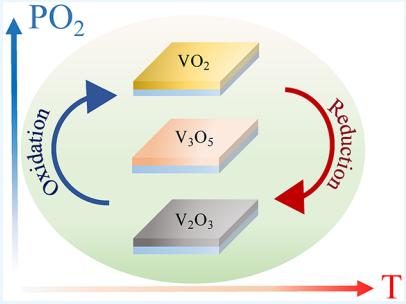

KEYWORDS: *vanadium oxide thin films, metal–insulator transition, high-vacuum annealing, phase diagram, oxygen stoichiometry, oxide electronics*

1. INTRODUCTION

Metal–insulator transitions (MITs) in oxides have been of special interest in condensed matter physics[1,2] and technology[3] in past decades. Specifically, vanadium oxides (VO_X) are considered very promising materials for next-generation oxide electronics. For instance, VO_2 has attracted much attention owing to its MIT near room temperature ($T_{MIT} \sim 340$ K), in which a large increase in electric resistivity is accompanied by a structural phase transition (SPT).[4,5] Additional interest in VO_2 concerns the possibility of modulating this transition by external stimuli.[6−8] The significant change in electrical resistivity offers a platform for resistive switching[9] and neuromorphic computation-[10−12] related applications. In pure and Cr-doped V_2O_3, the concurrence of metal–insulator, structural, and magnetic phase transitions has been the subject of much fundamental research.[13−16] The V_3O_5 phase, as one of the only two VO_X members with a MIT above room temperature ($T_{MIT} \sim 430$ K), is an excellent candidate for use in silicon-based technologies[17] and switching device applications.[18−20] During this MIT, the lattice structure remains monoclinic with a change in space group symmetry from $I2/c$ to $P2/c$. The possibility to trigger the MIT without a significant structural change is of great advantage for V_3O_5-based switching devices.

Vanadium oxides are very sensitive to changes in oxygen stoichiometry. Vanadium is a multivalent element displaying oxidation states between V^{2+} and V^{5+}, which gives rise to a series of compounds known as Magnéli (V_nO_{2n-1}) and Wadsley phases (V_nO_{2n+1}).[21−23] The existence of multiple phases leads to a complicated V–O phase diagram.[24−26] Furthermore, shrinking them into thin films or other nanoscale structures is needed to increase their functionality.[27] Typically, the V–O phase diagram is constructed with the thermodynamic data of bulk samples. However, as the size is reduced, the increase in the surface-to-volume ratio introduces an additional surface energy term in Gibbs-free energy that might affect the thermodynamically stable phase region.[28,29] Despite decades of research, a comprehensive understanding of thin-film thermodynamics in the VO_X system is still lacking. Most studies have only focused on the growth of VO_2 thin films and the improvement of their MIT properties by thermal annealing.[2,3,30−32] Other oxides such as V_3O_5, which is the

Received: October 12, 2020
Accepted: December 9, 2020
Published: December 22, 2020

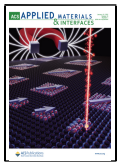

ACS Publications © 2020 American Chemical Society

https://dx.doi.org/10.1021/acsami.0c18327
ACS Appl. Mater. Interfaces 2021, 13, 887–896

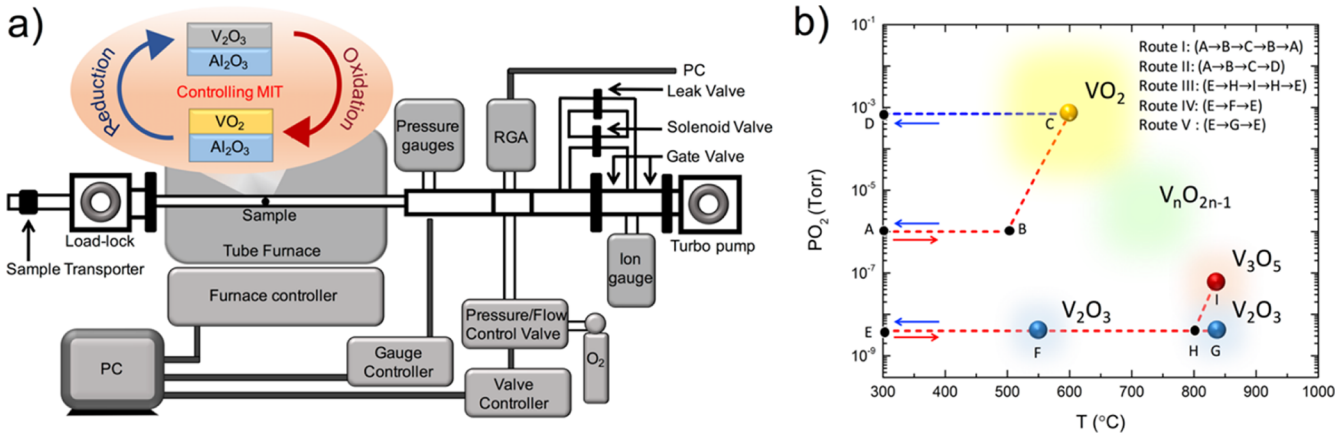

Figure 1. (a) Schematic illustration of the gas evolution setup used to control the oxygen stoichiometry in VO_X. (b) Synthesis pathways in the thermodynamic phase diagram of VO_X thin films. The dashed lines represent the different heating/cooling routes for preparing various phases of vanadium oxide.

closest Magnéli phase to V_2O_3, is particularly difficult to deposit directly because of the narrow range of allowable oxygen stoichiometry (with an O/V ratio between 1.666 and 1.668 ± 0.002).[33,34] The fabrication of V_3O_5 film in a recent work still contains a small amount of V_2O_3 impurities.[35] In general, obtaining high quality thin films of a specific VO_X and understanding the thin film phase diagram remain a challenging task.

In this study, we achieved control over oxygen stoichiometry in vanadium oxide thin films using a high-vacuum gas evolution system. The experimental setup is shown in Figure 1a. (See the Experimental Section for more details) We first sputtered VO_2 or V_2O_3 thin films on sapphire (α-Al_2O_3) substrates and then placed the samples in the center of a high vacuum tube furnace for heat treatment using high purity oxygen. A similar technique has been used to control oxygen deficiency in high-temperature superconducting $YBa_2Cu_3O_{7-X}$ samples.[36,37] Starting from single-phase VO_2 or V_2O_3 films, we are able to transform the initial material into a different VO_X film by carefully following a controlled route in the partial oxygen pressure (PO_2)−temperature (T) diagram (Figure 1b.). Various routes were tested to optimize the purity and enhance the MIT properties of the resulting compound. After treatment, the resulting phases were investigated using X-ray diffraction (XRD), reciprocal space mapping (RSM), X-ray photoelectron spectroscopy (XPS), and transport measurements. We show that our technique can provide excellent control over a wide range of temperatures and oxygen partial pressures down to high vacuum conditions, allowing us to minimize the effect of other gases or contaminations and increase the reproducibility of desired phases. This offers significant advantages over normal thermal oxidation/reduction methods using a gas mixture with a limited vacuum range (≥0.01 Torr).[38] The precision of our method is shown by obtaining single-phase V_3O_5 thin films with pronounced MIT despite their extremely narrow phase stability range. We are thus able to modulate the MITs between different phases and construct a detailed vanadium−oxygen phase diagram for thin VO_X films.

2. EXPERIMENTAL SECTION

2.1. Thin-Film Growth. Single-phase VO_2 and V_2O_3 thin films were deposited on 7 × 12 mm^2 (012) r-cut or (001) c-cut sapphire (α-Al_2O_3) substrates using RF magnetron sputtering from a V_2O_3 target. As described in previous studies,[9,41] the growth of VO_2 was done at a substrate temperature of 520 °C in an environment of Ar/O_2 mixture (8% O_2) at 3.7 mTorr. The V_2O_3 thin films were prepared at a 700 °C substrate temperature in an environment of ultrahigh purity Ar (>99.999%) at 8 mTorr.

2.2. Gas Evolution System. A high-vacuum oxygen annealing method was developed to synthesize complex oxide thin films with controlled oxygen stoichiometry. The experimental setup is shown in Figure 1a. The base pressure of the system is ∼1 × 10^{-7} Torr. Thin film samples were placed in the center of a Lindberg/Blue M 1200 °C tube furnace for heat treatment under different oxygen atmospheres. The PO_2 was measured using a residual gas analyzer equipped with a quadrupole mass spectrometer (UHV to 10^{-4} Torr) and two capacitance manometers (10^{-4} to 1000 Torr). A MKS series 245 pressure/flow control valve, a variable leak valve, and a solenoid valve were used to carefully control the PO_2. High-purity oxygen (>99.99%) was introduced into the annealing chamber using the computer-controlled metal-seated valve. This gas evolution setup provides a wide pressure range (UHV to 1000 Torr) and allows for the continuous variation of PO_2 under high vacuum conditions.

2.3. Evolution of V_2O_3 Phase into VO_2. Oxidation of as-deposited V_2O_3/Al_2O_3 (r-cut) thin films with 75 nm thickness was performed in the gas evolution system by continuously controlling PO_2 and T. The annealing conditions were chosen according to the known bulk vanadium−oxygen phase diagram.[24−26] By carefully following thermodynamically stable paths, different oxidation states of vanadium could be obtained from V_2O_3. At the start of route I (A → B → C → B → A) (see Figure 1b), PO_2 was fixed to 1 × 10^{-6} Torr, and the temperature was ramped up to 500 °C at a heating rate of 10 °C/min. After reaching 500 °C, the PO_2 was continuously increased along (B → C) in order to keep the sample in the potentially stable region of the VO_2 phase in the PO_2−T diagram. The sample was then annealed at 600 °C for 3 h with PO_2 ∼ 7 × 10^{-4} Torr (at point C in Figure 1b). After reaching thermodynamic equilibrium, both PO_2 and T were reduced at a cooling rate of 6 °C/min along the return path (C → B). After reaching 500 °C, the sample was then quenched to room temperature by transferring it to the load lock.

Similarly, by following route II (A → B → C → D), the oxygen stoichiometry in as-deposited V_2O_3 can be modified, leading to a transformation into a higher oxidation state. After a 3 h reaction at 600 °C (point C), the sample was cooled down to room temperature under continuous oxygen flow at PO_2 ∼ 7 × 10^{-4} Torr. As will be discussed later, this method produces high-quality VO_2 thin films with sharp MITs. The ability to continuously and gradually control both PO_2 and T is important for maintaining thermodynamic equilibrium in the thin film sample at all times so as to prevent the formation of possible secondary phases during the process.

https://dx.doi.org/10.1021/acsami.0c18327
ACS Appl. Mater. Interfaces 2021, 13, 887−896

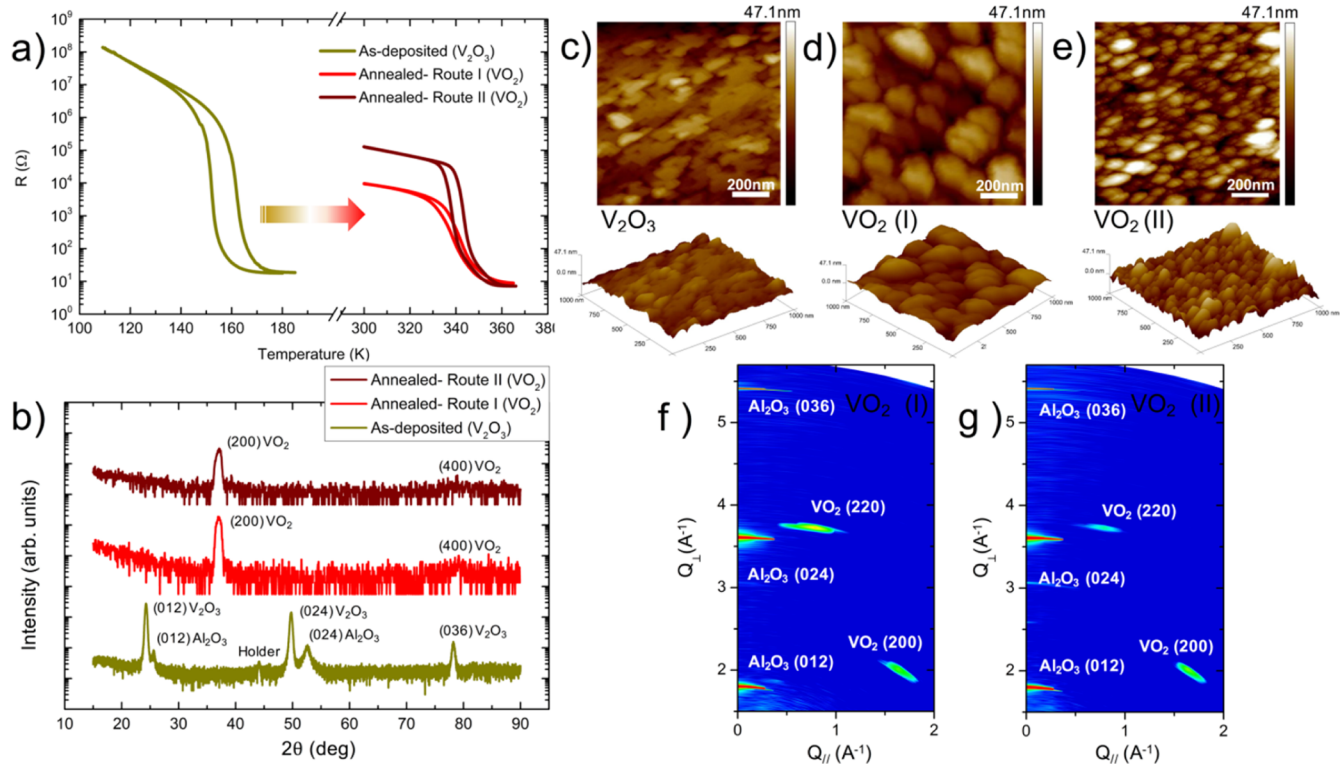

Figure 2. Formation of VO_2 phase from a V_2O_3 thin film on a (012) r-cut sapphire substrate. (a) Resistance vs temperature of vanadium oxide thin films under various oxidation conditions. After annealing, the thin films showed a sharp VO_2 MIT at ~340 K. (b) Room-temperature XRD scans for vanadium oxide films. The different diffraction spectra correspond to the V_2O_3 phase (as-deposited) and the VO_2 phase (annealed following route I or route II). The crystallographic orientation of the VO_2 film was (200), which points along ~40° to the surface normal ($\chi \sim 40°$). The angle (χ) denotes the degree between the surface normal and the diffraction plane. AFM images (1×1 μm^2) showing the surface morphology of the (c) as-deposited film, (d) (route I)-annealed film, and (e) (route II)-annealed film. The scale bar is 200 nm for all images. RSM of (f) (route I)-annealed and (g) (route II)-annealed VO_2 films. $Q_\perp$ denotes the out-of-plane orientation (012) of Al_2O_3.

2.4. Evolution of V_2O_3 Phase into V_3O_5. For the oxidation reaction of V_2O_3 into V_3O_5, we used a similar procedure. At the start of route III (E → H → I), the as-deposited V_2O_3/Al_2O_3 (c-cut) film with a thickness of approximately 100 nm was mounted on the tube furnace and the PO_2 was fixed to ~4×10^{-9} Torr. The temperature was then increased from RT to 800 °C at a rate of 10 °C/min (E → H). From point H, both the PO_2 and temperature (T) were continuously increased along the possible stable region for V_3O_5. The thin film was then annealed for 3 h at 838 °C with $PO_2 \sim 8 \times 10^{-8}$ Torr (at point I). After reaching phase equilibrium, both PO_2 and T were continuously reduced along the return route (I → H) at a cooling rate of 6 °C/min, and the sample was quenched from 800 °C to room temperature along the return path (H → E). In the case of V_2O_3/Al_2O_3 (r-cut) film, we performed the same experiment: the 100 nm film was annealed following route III. The annealing time was 3 h at point I in the first round and increased to 6 h for the second round.

2.5. Evolution of VO_2 Phase into V_2O_3. In order to understand the phase stability of VO_2, the as-deposited VO_2/Al_2O_3 (r-cut) films with a thickness of 75 nm were heat-treated under two different thermodynamic paths: route IV (E → F → E) and route V (E → G → E). At the start of route IV, the temperature was increased at a rate of 10 °C/min to 550 °C under $PO_2 \sim 4 \times 10^{-9}$ Torr. The annealing time was optimized to 12 h. After the reduction reaction, the sample was rapidly quenched in order to prevent the formation of other Magnéli phases that might occur during a slow cooling process. Similarly, along thermodynamic route V, the sample was stabilized at 838 °C for 12 h (point G) and also rapidly quenched to room temperature.

2.6. Characterization. Room-temperature θ−2θ XRD and RSM were used to characterize the lattice structure and its relation to the substrate structure using a Rigaku SmartLab X-ray diffractometer with Cu Kα radiation (λ = 1.54 Å). Atomic force microscopy for room-temperature surface characterization was performed using a Veeco scanning probe microscope. The scan area of each of the films was fixed to 1×1 μm^2. X-ray photoelectron spectroscopy (XPS) was carried out using a Kratos AXIS Ultra DLD XPS instrument equipped with an Al X-ray source and a 165 mm electron energy hemispherical analyzer. All the spectra were calibrated to the strongest O 1s component at 530.0 eV.[39,40] Samples were cleaned by Ar ion beam (4 keV) sputtering for 12 s prior to the measurements to remove the surface layer contamination. The N 1s, C 1s, and O 1s peaks and the V 2p peak were constantly monitored to prevent the peak distortion and the change in the oxidation state of vanadium ions.[39,40] Shirley background was used for the peak fitting. Temperature-dependent electrical transport measurements using a standard four-point probe configuration were performed using a Lakeshore TTPX probe station with a Keithley 6221 current source and a Keithley 2182A nanovoltmeter.

3. RESULTS AND DISCUSSION

3.1. V_2O_3 to VO_2. Figure 2a shows the electrical transport of V_2O_3/Al_2O_3 (r-cut) thin films before and after different gas evolution treatments. The R−T curve of as-deposited V_2O_3 shows a sharp MIT at $T_{MIT} \sim 160$ K, with at least 6 orders of magnitude change in the electrical resistance and a 10 K thermal hysteresis between the heating and cooling branches. The single-phase growth of the V_2O_3 thin film on r-cut sapphire is confirmed by the XRD scan shown in Figure 2b. The scattering intensity of V_2O_3 is much stronger than sapphire when the X-ray was aligned with the V_2O_3 peak. There are three out-of-plane diffraction peaks corresponding to (012), (024), and (036) corundum V_2O_3 phases. X-ray

https://dx.doi.org/10.1021/acsami.0c18327
ACS Appl. Mater. Interfaces 2021, 13, 887−896

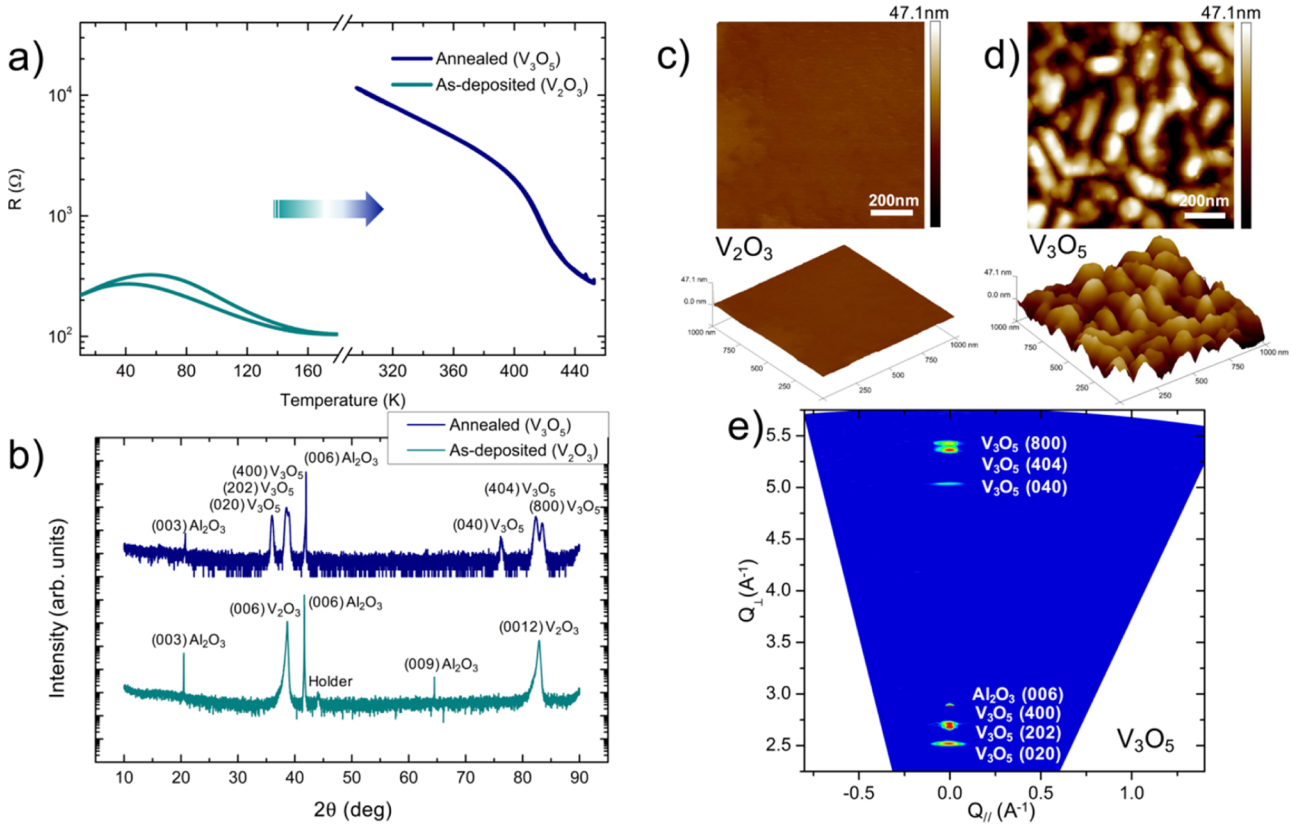

Figure 3. Formation of the V_3O_5 phase from a V_2O_3 thin film on a (001) c-cut sapphire substrate. (a) Resistance as a function of temperature of the V_2O_3 film and the resulting V_3O_5 film. The MIT temperature (T_{MIT}) of V_3O_5 is ∼ 417 K. (b) Room-temperature XRD scans. Evolution of different peaks corresponding to the V_2O_3 phase (as-deposited) and the V_3O_5 phase (annealed following route III). Preferred crystallographic orientations of the V_3O_5 film were (020), (202), and (400). AFM images revealed the surface morphology of (c) as-deposited film and (d) (route III)-annealed film. (e) X-ray RSM of the resulting V_3O_5 film. $Q_\perp$ denotes the out-of-plane orientation (001) of Al_2O_3 (perpendicular to the film surface).

measurements on similar films[41] suggest that V_2O_3 grows epitaxially along the crystallographic orientation of the (012) sapphire substrate. By following the annealing process (route I) in the PO_2-T phase diagram (Figure 1b), this film was transformed into VO_2, with 3 orders of magnitude MIT at T_{MIT} ∼ 340 K (Figure 2a). Interestingly, this MIT was significantly improved and enhanced by following route II. The resulting VO_2 phase was confirmed by RSM (see Figure 2f,g). The absence of diffraction peaks from other Magnéli phases indicates the formation of single-phase VO_2 films.

Figure 2b shows the XRD spectra for (route I)-annealed and (route II)-annealed samples. XRD patterns for samples subjected to both routes clearly show the diffraction peak at 37.1°, corresponding to the (200) plane of the VO_2 monoclinic structure. The resulting VO_2 films still exhibit the preferred orientation with the (200) plane pointing at ∼40° to the surface normal ($\chi \sim 40°$), while for the directly sputtered VO_2 films on r-cut sapphire, the (200) plane is parallel to the substrate surface ($\chi \sim 0°$) (Figure 4b). The formation of a tilted (200) plane indicates the lack of well-aligned epitaxial layers and the appearance of disorder at the VO_2/Al_2O_3 interface, as present in many oxide heterostructures.[42] It should be noted that there are structural similarities between rutile VO_2 and corundum V_2O_3. Previous studies have shown that through a common parent structure with a hexagonal-close-packing arrangement, VO_2 and V_2O_3 may be derived from each other through a well-defined symmetry-breaking mechanism along the [001] direction of corundum V_2O_3 and the [100] of rutile VO_2.[43] It is thus unlikely that the formation of VO_2 from V_2O_3 would be randomly oriented.

The AFM images demonstrate the differences in surface morphology and roughness between the as-deposited V_2O_3 (Figure 2c), (route I)-annealed film (Figure 2d), and (route II)-annealed film (Figure 2e). The root-mean-square roughness extracted from Figure 2c−e was 5.62, 6.22, and 8.29 nm, respectively. The original V_2O_3 film prepared by sputtering reveals a relatively smooth surface. The quenching process along route I results in a bigger grain size (∼190 nm assuming a spherical shape) of the VO_2 film. It is this (route I)-annealed VO_2 film that exhibits a smaller width in the hysteresis loop appearing in the $R-T$ curve at the MIT (Figure 2a). Consequently, our results suggest that the hysteresis loop at the MIT broadens with decreasing grain size.[44,45] Earlier reports show that smaller grains lead to a high density of grain boundaries, resulting in a decrease in the magnitude of the resistivity change across the MIT.[46] Alternatively, the larger resistance switching ratios and smaller grains (∼75 nm) observed in the (route II)-annealed VO_2 film suggest that the change in the electrical resistance cannot be solely due to a grain size effect. Oxygen stoichiometry must also play a role in the MIT behavior of VO_2. The activation energy (E_a) of the VO_2 insulating state ($T \leq 310$ K) can be estimated from the linear fitting of the ratio $\ln R(T)/(1/k_bT)$, as $R(T) = R_0 \exp(E_a/k_bT)$. The results obtained from (route I)-annealed and (route II)-annealed VO_2 are ∼191 and ∼259 meV, respectively. Quenching the (route I)-annealed VO_2 film

https://dx.doi.org/10.1021/acsami.0c18327
ACS Appl. Mater. Interfaces 2021, 13, 887−896

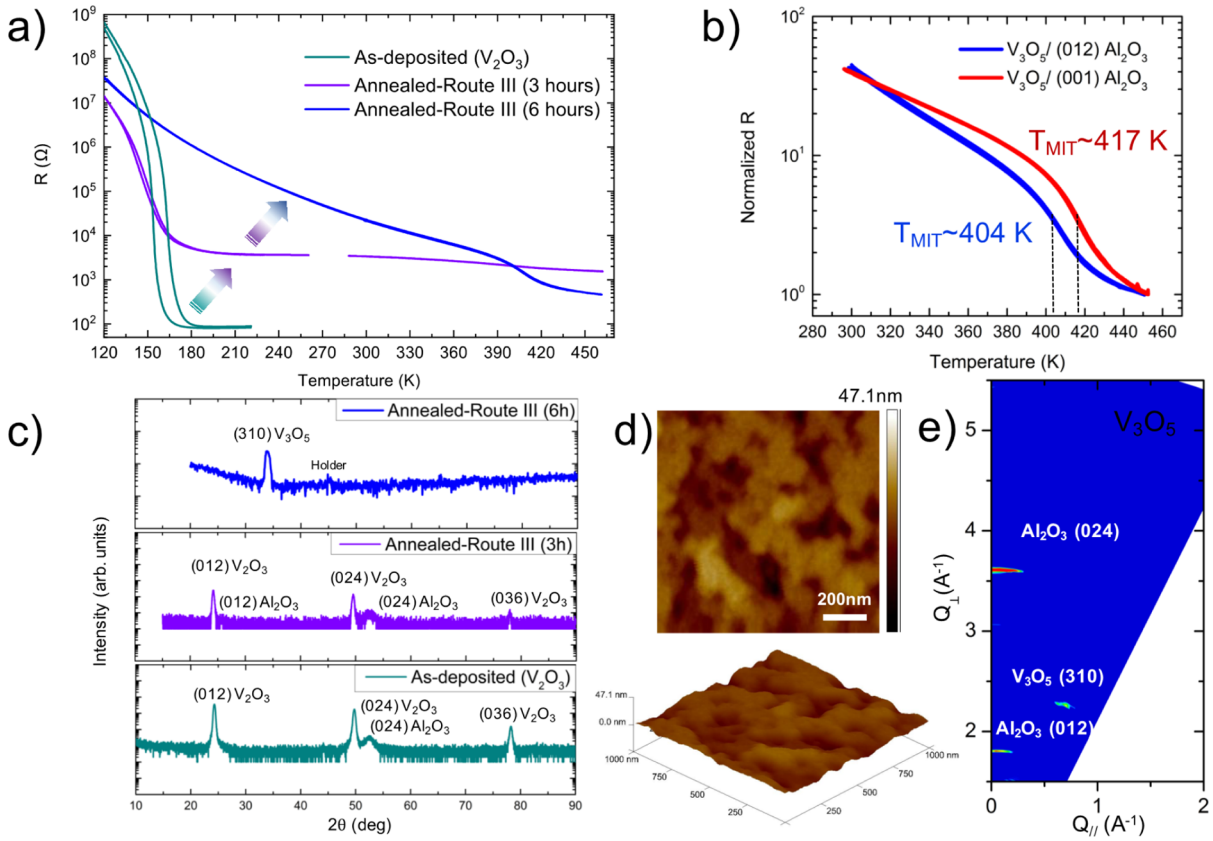

Figure 4. Formation of the V_3O_5 phase from a V_2O_3 thin film on a (012) r-cut sapphire substrate. (a) Resistance as a function of temperature for a V_2O_3 film: as-deposited film (cyan); after annealing for 3 h at point I (purple); and after annealing for additional 6 h at point I (blue). (b) Comparison of the normalized $R(T)$ for V_3O_5 films on r-cut sapphire (blue) and c-cut sapphire (red). The black dashed lines mark the T_{MIT} for the two different samples. (c) XRD measurements of samples after time-annealed V_2O_3 thin film following route III. The preferred crystallographic orientation of the resulting V_3O_5 film was (310), which points along ~17° to the surface normal ($\chi \sim 17°$). (d) AFM images revealing the surface morphology and (e) X-ray RSM of the resulting V_3O_5 film. $Q_\perp$ denotes the out-of-plane orientation (012) of Al_2O_3 (perpendicular to the film surface).

under relatively low PO_2 is likely to increase the density of defects and promote oxygen loss. These vacancies may dope the VO_2, thus increasing the free carriers and reducing the resistive change across the MIT.[47,48] A detailed phase stability diagram (Figure 7.) also shows that annealing the sample at 600 °C with a low oxygen pressure will result in oxygen-deficient VO_{2-x} phases.

3.2. V_2O_3 to V_3O_5. Because of the numerous possible oxidation states, vanadium oxides are very sensitive to changes in the oxygen content. Here, we show that oxidation of V_2O_3 to form V_3O_5 can be achieved on c-cut and r-cut sapphire by slightly increasing the PO_2 at ~840 °C. Figure 3a displays the temperature-dependent electrical transport of a V_2O_3 film grown on c-cut sapphire before and after the gas evolution treatment. The $R-T$ curve of the as-deposited V_2O_3 film shows a suppressed MIT with only a slight resistance variation. We note that this V_2O_3 sample was grown under the same conditions as the one shown in Figure 2a, which shows a much more pronounced MIT. This suppression of the MIT in V_2O_3 grown on c-cut sapphire had been previously attributed to the strain and microstructural effects between the thin film and substrate.[49,50] The lattice parameters and the c/a ratio of our epitaxial c-cut V_2O_3 thin film are ~2.81 ($a = b = 4.98$ Å; $c = 14.01$ Å). This ratio is consistent with the reported value of c-cut V_2O_3 with unusual metal−insulator−metal behavior.[49] In previous work, we have shown that the SPT and MIT were robustly coupled to each other.[16] Therefore, it is likely that the SPT in our V_2O_3 sample is highly dependent on the a- and c-axis deformation as well. This leads to the suppression of the MIT. The XRD pattern in Figure 3b shows that the corundum V_2O_3 film is highly oriented with the (001) c-cut sapphire substrate. By annealing this film along route III (Figure 1b), we were able to transform it into a single-phase V_3O_5 film with an MIT of more than 1 order of magnitude at $T_{MIT} \sim 417$ K. The smooth MIT behavior above room temperature together with the absence of thermal hysteresis in $R(T)$ are signs of a second-order phase transition, as reported before.[18,51]

The presence of a single-phase polycrystalline structure is confirmed by RSM, as shown in Figure 3e. The axis $Q_\perp$ points along the out-of-plane orientation (001) for the Al_2O_3 substrate. Figure 3b shows six diffraction peaks at $2\theta = 36.0$, 38.5, 38.9, 76.2, 82.3, and 83.4° corresponding to the (020), (202), (400), (040), (404), and (800) planes in V_3O_5, respectively.[52] All the observed peaks shifted slightly to higher values of 2θ (i.e., the d-spacing for each plane is contracted) with respect to the bulk values. This implies that residual strains were induced in the film after recrystallization. If annealing was interrupted before complete transformation, crystalline V_2O_3 and V_3O_5 phase coexistence could be observed. The AFM image of the as-deposited V_2O_3 film (Figure 3c) indicates a relatively smooth film surface with 0.72 nm RMS roughness. The resulting V_3O_5 film shown in Figure

https://dx.doi.org/10.1021/acsami.0c18327
ACS Appl. Mater. Interfaces 2021, 13, 887−896

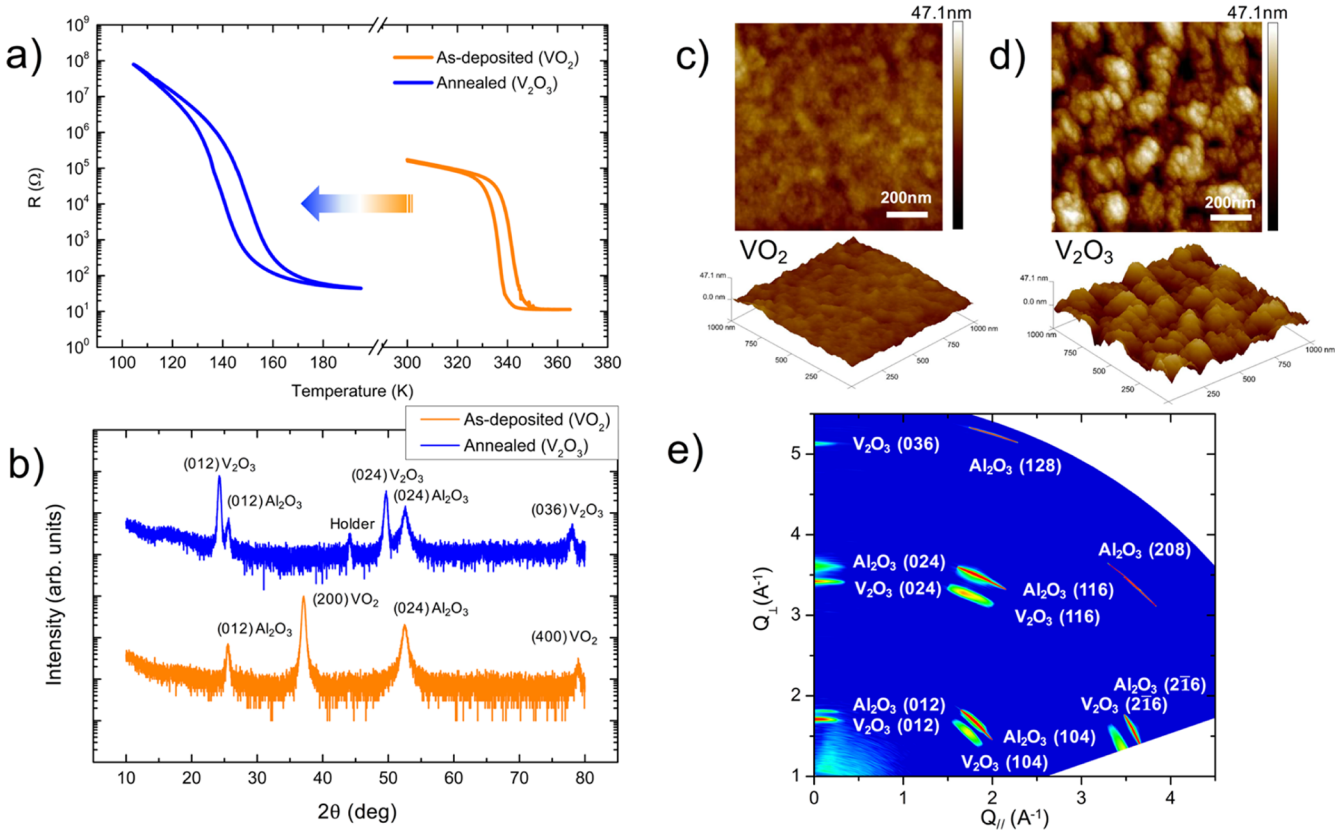

Figure 5. Formation of the V_2O_3 phase from the VO_2 thin film on a (012) r-cut sapphire substrate. (a) Resistance as a function of temperature of the VO_2 film and the resulting V_2O_3 film. (b) Room-temperature XRD scans. Evolution of different peaks corresponding to the VO_2 phase (as-deposited) and the V_2O_3 phase (following annealing route IV). AFM images revealed the surface morphology of (c) as-deposited film and (d) annealed film. (e) Wide-range RSM of the transformed V_2O_3 film. Both in-plane and out-of-plane crystallographic orientations of the V_2O_3 film strongly followed the r-cut sapphire substrate orientations, suggesting the formation of epitaxial structures after gas evolution. $Q_\perp$ denotes the out-of-plane orientation (012) of Al_2O_3.

3d has a much rougher surface with 13.1 nm RMS roughness. Furthermore, the grain structure is highly irregular after the treatment, as suggested by the XRD and RSM data.

Figure 4a demonstrates the electrical transport of a V_2O_3 film on r-cut sapphire before and after gas evolution treatments along route III. After annealing at point I for 3 h, we observe an increase in the resistance in the metallic states and a reduction of the magnitude of the hysteresis. However, the large MIT at $T_{MIT} \sim 150$ K indicates that the major phase of the film is still V_2O_3. The formation of a pure V_3O_5 phase is achieved by a second annealing process for additional 6 h along route III. The $R(T)$ starts showing a smooth MIT above room temperature ($T_{MIT} \sim 404$ K) without thermal hysteresis. A comparison of $R-T$ curves of V_3O_5 films grown on c-cut (001) and r-cut (012) Al_2O_3 substrates is shown in Figure 4b. Both samples reveal an MIT of more than 1 order of magnitude. For ease of comparison, the results were normalized by the metallic state resistance (R_{450K}). As the transformed V_3O_5 films were polycrystalline, it is likely that the strain in the different grains is highly inhomogeneous. Different sapphire substrates will generate different dislocations and strain. Because of the numerous grain orientations, it is quite challenging to precisely quantify the strain in the polycrystalline thin film. By comparing the lattice spacings in V_3O_5 grown on r-cut and c-cut oriented sapphire, the structural distortion can still be estimated. Compared with the c-cut V_3O_5 thin film, the relative strains for the (100), (010), and (001) planes of V_3O_5/r-cut sapphire are considerably more compressed ($\Delta d_{100} \sim -0.71\%$; $\Delta d_{010} \sim 0.03\%$; $\Delta d_{001} \sim -2.1\%$). It is likely that a larger compressive strain leads to a lower T_{MIT} as found in a previous study, which has shown that T_{MIT} in V_3O_5 decreases with pressure.[53] The strain generated from the sapphire substrates and the difference in microstructure and grains might lead to the 14 K variation in T_{MIT}. Figure 4c shows the evolution of the crystalline structure for the V_2O_3 film. After 3 h of annealing, the intensity of the diffraction peaks decreased, but the thin film still remained as corundum V_2O_3. On the other hand, the second, lengthier annealing time (6 h) allowed for a complete transformation into V_3O_5. Besides the out-of-plane sapphire peaks, several in-plane V_3O_5 peaks can be found using RSM. For instance, one diffraction peak from the V_3O_5 (310) plane was found at $\chi \sim 17°$ (Figure 4c,e). The RMS roughness of the transformed V_3O_5 film is 4.21 nm (Figure 4d).

Interestingly, a large difference in the annealing times required to form V_3O_5 is observed for the two different substrates, (012) and (001) Al_2O_3. This indicates that the crystallographic orientation of the film significantly affects the thermodynamic kinetics and oxygen diffusion processes. As we observe from our XRD measurements (Figures 3b and 4c), for both substrates, in the final stage, the samples only showed diffraction peaks associated with V_3O_5 (aside from the sapphire peaks) indicating high phase purity.

3.3. VO_2 to V_2O_3. In addition to the controlled oxidation of as-grown V_2O_3 thin films using the gas evolution technique

https://dx.doi.org/10.1021/acsami.0c18327
ACS Appl. Mater. Interfaces 2021, 13, 887−896

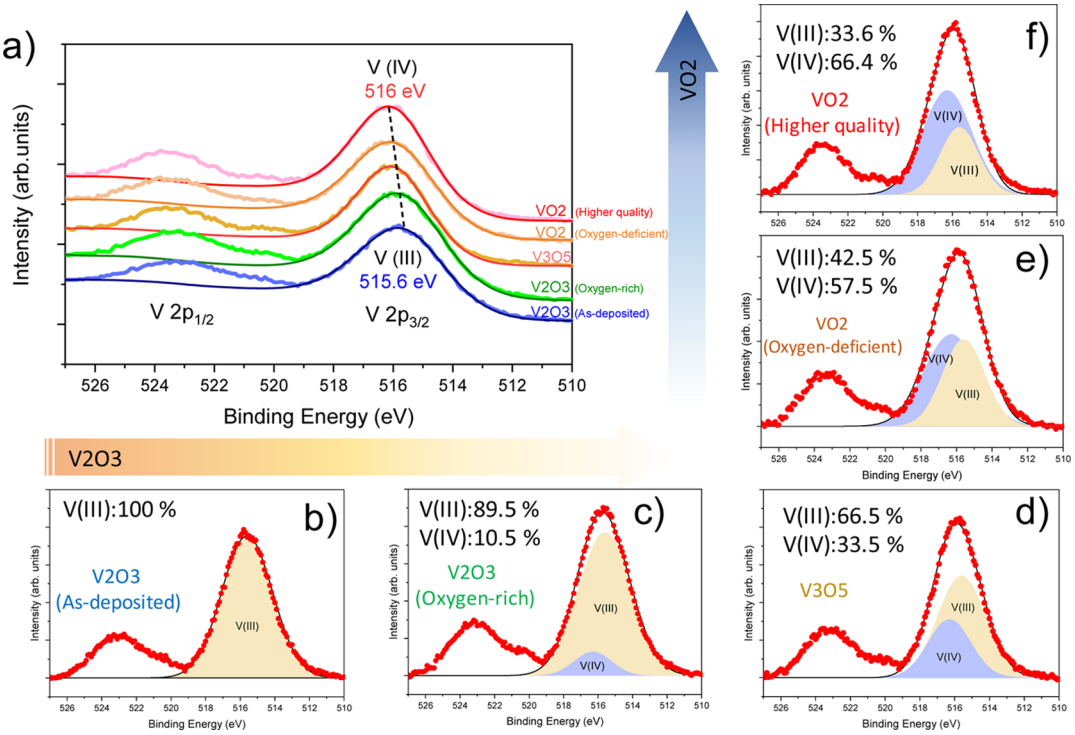

Figure 6. XPS spectra of vanadium oxide thin films. (a) V 2p spectra in the range of 510−526 eV. Spectra of (b) as-deposited V_2O_3 film; (c) (route IV)-annealed film, oxygen-rich V_2O_3 phase; (d) (route III)-annealed film, V_3O_5 phase; (e) (route I)-annealed film, oxygen-deficient VO_2 phase; and (f) (route II)-annealed film, higher quality VO_2 phase.

described above, we have also demonstrated and studied the controlled reduction of as-grown VO_2 thin films on r-cut sapphire to study the thin-film phase stability. Figure 5a shows the electrical transport of a VO_2 film on an r-cut sapphire both before and after the gas evolution treatments along route IV. The $R-T$ curve of as-deposited VO_2 shows a sharp MIT at $T_{MIT} \sim 340$ K, with more than 3 orders of magnitude resistance change. The single-phase growth of VO_2 is confirmed by the XRD scan shown in Figure 5b. Two reflection peaks corresponding to the (200) and (400) planes for monoclinic VO_2 are observed at $2\theta = 37.1$ and 79.0°, respectively. By following the annealing process (route IV) shown in Figure 1b, the highly textured VO_2 film was transformed into single-phase V_2O_3, now with 5 orders of magnitude MIT with $T_{MIT} \sim 145$ K (see Figure 5a). This value of transition temperature $T_{MIT} \sim 145$ K is slightly lower than the value of the transition temperature $T_{MIT} \sim 160$ K, for the directly sputtered V_2O_3 film, indicating that there might be a comparatively higher oxygen concentration in the transformed V_2O_3 film.[54] Moreover, we find no significant differences ($\Delta 2\theta \leq 0.035°$) in the out-of-plane (012) and in-plane (104) XRD peaks between directly sputtered V_2O_3 and transformed V_2O_3 films, ruling out strain effects as a major cause for the decrease in T_{MIT}. Previous studies on V_2O_3 have shown that a 15 K variation in T_{MIT} corresponds to an excess of oxygen concentration.[55,56] The presence of an epitaxial V_2O_3 film was confirmed by XRD (Figure 5b) and RSM scans (Figure 5e). Both in-plane and out-of-plane crystallographic orientations in V_2O_3 follow the substrate orientations. This indicates that the structural similarity between corundum V_2O_3 and Al_2O_3 promotes epitaxial growth during the atomic rearrangement. Therefore, it is reasonable to conclude that the coupling to the Al_2O_3 substrate plays an important role in determining the crystallographic orientations of the transformed film. We note that this is in contrast with the case of VO_2 derived from a V_2O_3 film, which develops a different orientation after gas evolution compared to the as-grown VO_2 film. This may be due to the higher degree of compatibility between the Al_2O_3 substrate and the isostructural V_2O_3 compared to the rutile VO_2.

For the transformation of as-grown VO_2 films into single-phase V_2O_3, it takes 12 h (point F in the PO_2-T diagram shown in Figure 1b) to reach an equilibrium state. We found that the as-grown VO_2 films that were subjected to a shortened annealing process of only 3 or 6 h along route IV did not exhibit any clear MIT behavior, and no XRD peaks can be found. This suggests that thermodynamic equilibrium may not have been reached in this shorter period of time. However, the reverse transformation of as-grown V_2O_3 films into single-phase VO_2 films requires a shorter annealing time of 3 h. The discrepancy between these two cases suggests that the phase evolution mechanisms are also associated with the kinetic and diffusion processes, which are beyond the scope of this work. Furthermore, the monoclinic VO_2 film could also be transformed into corundum V_2O_3 phase by following an alternate annealing treatment along route V. This indicates that point G in Figure 1b is still in the V_2O_3 stable region. Figure 5c,d shows the surface morphology of the as-deposited film and (route IV)-annealed film, respectively. The VO_2 film prepared by sputtering shows a textured surface with the RMS roughness equal to 3.15 nm. The resulting V_2O_3 after the loss of oxygen shows a relatively rougher surface with roughness up to 8.35 nm.

XPS was used to track the valence state of the as-deposited and annealed thin films on the (012) sapphire substrate described above. The binding energy (BE) calibration was

https://dx.doi.org/10.1021/acsami.0c18327
ACS Appl. Mater. Interfaces 2021, 13, 887−896

done for the O 1s peak at 530 eV.[40,57] Shirley background was used for the peak fitting. The V 2p spectra in the range of 510−526 eV show the spin−orbit splitting peak of V $2p_{3/2}$ and V $2p_{1/2}$ (Figure 6a). Only one component V(III) centered at 515.6 eV was used for the as-deposited V_2O_3 spectrum (Figure 6b), as the peak shape is symmetric (V $2p_{3/2}$ at 515.6 eV for +3 valence state).[58] The energy difference between O 1s and V $2p_{3/2}$ is 14.4 eV, well in the range of the reported value for single crystals.[58] With increasing oxygen content in thin films, the position of the V $2p_{3/2}$ peak shifts from V(III) at 515.6 to 516.0 eV. Similar behavior was reported previously for single crystals.[58,59] We find an increase in the V 2p BE from V_2O_3 (as-deposited film) to V_2O_3 (route IV-annealed film), V_3O_5 (route III-annealed film), VO_2 (route I-annealed film), and VO_2 (route II-annealed film). Each V $2p_{3/2}$ peak can be deconvoluted into V(III) and V(IV) states centered at 515.6 and 516.3 eV, respectively (V $2p_{3/2}$ at 516.3 eV for +4 valence; BE difference between O 1s and V $2p_{3/2}$ ∼ 13.7 eV).[58] The fitting area of V $2p_{3/2}$ could be used to track the oxidation states of vanadium ions. The estimated V(III)/V(IV) ratio in the V_3O_5 thin film is 66.5:33.5% (Figure 6c). The valence state of vanadium is around +3.34, which is close to the theoretical value of +3.3. On the other hand, the (route I)-annealed film (VO_2 phase) contains higher oxygen vacancies and shows a higher V(III) component in Figure 6e. This confirms that quenching the VO_2 under relatively low PO_2 will lead to oxygen loss. It should be noted that the (route II)-annealed VO_2 film still shows a small portion of V(III) charge, indicating that there are still some oxygen vacancies in this transformed VO_2 film near the surface. It is thus possible to achieve higher quality VO_2 thin films under higher PO_2 annealing conditions.

Our technique can provide excellent control over a wide range of temperatures and oxygen partial pressures, allowing us to explore a more complete picture of thin-film phase diagram. It is worth noting that the V−O phase diagram (Figure 7) we obtain starting from 100 nm V_2O_3 is substantially different from the bulk V−O phase diagram.[24−26] At the present stage, among all the Magnéli phases, the only thin film we could obtain in the pure form was V_3O_5. It is possible to fabricate other Magnéli-phase thin film using our technique despite their extremely narrow phase stability range. Moreover, starting from 10 nm ultrathin films, despite tens of trials, we could not obtain the V_3O_5 phase under the same annealing conditions. These differences in conditions as compared to those of the bulk phase diagram may be due to variations in nanoscale surface energy and the lattice interaction with the substrate. This may also explain the differences in the required annealing time found for sapphire substrates of different orientations (c-cut and r-cut), as described above.

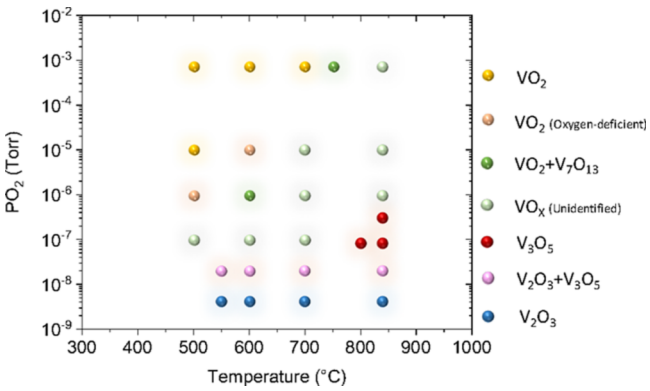

Figure 7. V−O phase diagram for a thin film. Circles represent the tested annealing conditions.

4. CONCLUSIONS

In summary, we have developed a high-vacuum gas evolution technique that allows for the precise modification of oxygen stoichiometry in VO_X thin films. Using temperature-dependent electrical transport measurements, XRD, RSM, and XPS, we show that optimal oxygen stoichiometry is obtained in each of the transformed films. Based on our technique, the thermodynamic phase diagram can be well-defined and elucidated for the V−O system when scaling down the VO_X from the bulk into a thin film form. Our results may play an important role in improving and controlling the transport properties across the MIT in oxide-based devices. It may open a new way to synthesize exotic or Magnéli phase oxide films, which cannot be directly grown by standard deposition techniques. We hope our work will encourage the use of gas evolution methods in other complex oxide systems.

■ AUTHOR INFORMATION

Corresponding Author

Min-Han Lee − *Materials Science and Engineering, University of California San Diego, La Jolla, California 92093, United States; Department of Physics and Center for Advanced Nanoscience, University of California San Diego, La Jolla, California 92093, United States;* orcid.org/0000-0001-9093-4891; Email: mil006@eng.ucsd.edu

Authors

Yoav Kalcheim − *Department of Physics and Center for Advanced Nanoscience, University of California San Diego, La Jolla, California 92093, United States;* orcid.org/0000-0002-1489-0505

Javier del Valle − *Department of Physics and Center for Advanced Nanoscience, University of California San Diego, La Jolla, California 92093, United States*

Ivan K. Schuller − *Materials Science and Engineering, University of California San Diego, La Jolla, California 92093, United States; Department of Physics and Center for Advanced Nanoscience, University of California San Diego, La Jolla, California 92093, United States*

Complete contact information is available at: https://pubs.acs.org/10.1021/acsami.0c18327

Notes

The authors declare no competing financial interest.

■ ACKNOWLEDGMENTS

The initial development of oxides was supported by the Vannevar Bush Faculty Fellowship program, sponsored by the Basic Research Office of the Assistant Secretary of Defense for Research and Engineering and funded by the Office of Naval Research through grant N00014-15-1-2848, and by collaborative NSF under grants DMR 1805585 and DMR 1804414. The synthesis and structural studies of V_3O_5 were funded by the Air Force Office of Scientific Research under award number FA9550-20-1-0242.The XPS measurements were carried out at ACIF in University of California, Riverside supported by NSF under grant DMR 0958796.

https://dx.doi.org/10.1021/acsami.0c18327
ACS Appl. Mater. Interfaces 2021, 13, 887−896

REFERENCES

(1) Imada, M.; Fujimori, A.; Tokura, Y. Metal-Insulator Transitions. *Rev. Mod. Phys.* **1998**, *70*, 1039−1263.

(2) Ngai, J. H.; Walker, F. J.; Ahn, C. H. Correlated Oxide Physics and Electronics. *Annu. Rev. Mater. Res.* **2014**, *44*, 1−17.

(3) Yang, Z.; Ko, C.; Ramanathan, S. Oxide Electronics Utilizing Ultrafast Metal-Insulator Transitions. *Annu. Rev. Mater. Res.* **2011**, *41*, 337−367.

(4) Lee, D.; Lee, J.; Song, K.; Xue, F.; Choi, S.-Y.; Ma, Y.; Podkaminer, J.; Liu, D.; Liu, S.-C.; Chung, B.; Fan, W.; Cho, S. J.; Zhou, W.; Lee, J.; Chen, L.-Q.; Oh, S. H.; Ma, Z.; Eom, C.-B. Sharpened VO_2 Phase Transition via Controlled Release of Epitaxial Strain. *Nano Lett.* **2017**, *17*, 5614−5619.

(5) Morin, F. J. Oxides Which Show a Metal-to-Insulator Transition at the Neel Temperature. *Phys. Rev. Lett.* **1959**, *3*, 34−36.

(6) Jeong, J.; Aetukuri, N.; Graf, T.; Schladt, T. D.; Samant, M. G.; Parkin, S. S. P. Suppression of Metal−Insulator Transition in VO_2 by Electric Field-Induced Oxygen Vacancy Formation. *Science* **2013**, *339*, 1402−1405.

(7) Cao, J.; Gu, Y.; Fan, W.; Chen, L. Q.; Ogletree, D. F.; Chen, K.; Tamura, N.; Kunz, M.; Barrett, C.; Seidel, J.; Wu, J. Extended Mapping and Exploration of the Vanadium Dioxide Stress-Temperature Phase Diagram. *Nano Lett.* **2010**, *10*, 2667−2673.

(8) Cavalleri, A.; Dekorsy, Th.; Chong, H. H. W.; Kieffer, J. C.; Schoenlein, R. W. Evidence for a Structurally-Driven Insulator-to-Metal Transition in VO_2: A View from the Ultrafast Timescale. *Phys. Rev. B: Condens. Matter Mater. Phys.* **2004**, *70*, 161102.

(9) del Valle, J.; Kalcheim, Y.; Trastoy, J.; Charnukha, A.; Basov, D. N.; Schuller, I. K. Electrically Induced Multiple Metal-Insulator Transitions in Oxide Nanodevices. *Phys. Rev. Appl.* **2017**, *8*, 054041.

(10) Zhou, Y.; Ramanathan, S. Mott Memory and Neuromorphic Devices. *Proc. IEEE* **2015**, *103*, 1289−1310.

(11) del Valle, J.; Salev, P.; Tesler, F.; Vargas, N. M.; Kalcheim, Y.; Wang, P.; Trastoy, J.; Lee, M.-H.; Kassabian, G.; Ramírez, J. G.; Rozenberg, M. J.; Schuller, I. K. Subthreshold Firing in Mott Nanodevices. *Nature* **2019**, *569*, 388−392.

(12) del Valle, J.; Ramírez, J. G.; Rozenberg, M. J.; Schuller, I. K. Challenges in Materials and Devices for Resistive-Switching-Based Neuromorphic Computing. *J. Appl. Phys.* **2018**, *124*, 211101.

(13) Held, K.; Keller, G.; Eyert, V.; Vollhardt, D.; Anisimov, V. I. Mott-Hubbard Metal-Insulator Transition in Paramagnetic V_2O_3: An LDA + DMFT(QMC) study. *Phys. Rev. Lett.* **2001**, *86*, 5345−5348.

(14) McWhan, D. B.; Rice, T. M.; Remeika, J. P. Mott Transition in Cr-Doped V_2O_3. *Phys. Rev. Lett.* **1969**, *23*, 1384−1387.

(15) Ramirez, J. G.; Saerbeck, T.; Wang, S.; Trastoy, J.; Malnou, M.; Lesueur, J.; Crocombette, J.-P.; Villegas, J. E.; Schuller, I. K. Effect of Disorder on the Metal-Insulator Transition of Vanadium Oxides: Local Versus Global Effects. *Phys. Rev. B: Condens. Matter Mater. Phys.* **2015**, *91*, 205123.

(16) Kalcheim, Y.; Butakov, N.; Vargas, N. M.; Lee, M.-H.; del Valle, J.; Trastoy, J.; Salev, P.; Schuller, J.; Schuller, I. K. Robust Coupling between Structural and Electronic Transitions in a Mott Material. *Phys. Rev. Lett.* **2019**, *122*, 057601.

(17) Jaramillo, R.; Schoofs, F.; Ha, S. D.; Ramanathan, S. High Pressure Synthesis of $SmNiO_3$ Thin Films and Implications for Thermodynamics of the Nickelates. *J. Mater. Chem. C* **2013**, *1*, 2455−2462.

(18) Kumar, N.; Rúa, A.; Lu, J.; Fernández, F.; Lysenko, S. Ultrafast Excited-State Dynamics of V_3O_5 as a Signature of a Photoinduced Insulator-Metal Phase Transition. *Phys. Rev. Lett.* **2017**, *119*, 057602.

(19) Fisher, B.; Patlagan, L.; Chashka, K. B.; Makarov, C.; Reisner, G. M. V_3O_5: Insulator-Metal Transition and Electric-Field-Induced Resistive-Switching. *Appl. Phys. Lett.* **2016**, *109*, 103501.

(20) Lee, D.; Park, J.; Park, J.; Woo, J.; Cha, E.; Lee, S.; Moon, K.; Song, J.; Koo, Y.; Hwang, H. Structurally Engineered Stackable and Scalable 3D Titanium-Oxide Switching Devices for High-Density Nanoscale Memory. *Adv. Mater.* **2015**, *27*, 59−64.

(21) Schwingenschlögl, U.; Eyert, V. The Vanadium Magnéli Phases V_nO_{2n-1}. *Ann. Phys.* **2004**, *13*, 475−510.

(22) Kosuge, K. The Phase Diagram and Phase Transition of the V_2O_3-V_2O_5 System. *J. Phys. Chem. Solids* **1967**, *28*, 1613−1621.

(23) Griffiths, C. H.; Eastwood, H. K. Influence of Stoichiometry on the Metal-Semiconductor Transition in Vanadium Dioxide. *J. Appl. Phys.* **1974**, *45*, 2201−2206.

(24) Kang, Y.-B. Critical Evaluation and Thermodynamic Optimization of the VO−$VO_{2.5}$ System. *J. Eur. Ceram. Soc.* **2012**, *32*, 3187−3198.

(25) Haber, J.; Witko, M.; Tokarz, R. Vanadium Pentoxide I. Structures and Properties. *Appl. Catal., A* **1997**, *157*, 3−22.

(26) Brückner, W.; Oppermann, H.; Reichelt, W.; Terukow, J. I.; Tschudnowski, F. A.; Wolf, E. *Vanadiumoxide*; Akademie-Verlag: Berlin, 1983.

(27) Liu, K.; Lee, S.; Yang, S.; Delaire, O.; Wu, J. Recent Progresses on Physics and Applications of Vanadium Dioxide. *Mater. Today* **2018**, *21*, 875−896.

(28) Navrotsky, A.; Ma, C.; Lilova, K.; Birkner, N. Nanophase Transition Metal Oxides Show Large Thermodynamically Driven Shifts in Oxidation-Reduction Equilibria. *Science* **2010**, *330*, 199−201.

(29) Navrotsky, A. Nanoscale Effects on Thermodynamics and Phase Equilibria in Oxide Systems. *ChemPhysChem* **2011**, *12*, 2207−2215.

(30) Rathi, S.; Lee, I.-Y.; Park, J.-H.; Kim, B.-J.; Kim, H.-T.; Kim, G.-H. Postfabrication Annealing Effects on Insulator−Metal Transitions in VO_2 Thin-Film Devices. *ACS Appl. Mater. Interfaces* **2014**, *6*, 19718−19725.

(31) Dou, Y.-K.; Li, J.-B.; Cao, M.-S.; Su, D.-Z.; Rehman, F.; Zhang, J.-S.; Jin, H.-B. Oxidizing Annealing Effects on VO_2 Films with Different Microstructures. *Appl. Surf. Sci.* **2015**, *345*, 232−237.

(32) Van Bilzen, B.; Homm, P.; Dillemans, L.; Su, C.-Y.; Menghini, M.; Sousa, M.; Marchiori, C.; Zhang, L.; Seo, J. W.; Locquet, J.-P. Production of VO_2 Thin Films through Post-Deposition Annealing of V_2O_3 and VO_x Films. *Thin Solid Films* **2015**, *591*, 143−148.

(33) Chudnovskii, F. A.; Terukov, E. I.; Khomskii, D. I. Insulator-Metal Transition in V_3O_5. *Solid State Commun.* **1978**, *25*, 573−577.

(34) Terukov, E. I.; Chudnovskii, F. A.; Reichelt, W.; Oppermann, H.; Brückner, W.; Brückner, H.-P.; Moldenhauer, W. Investigation of the Physical Properties of V_3O_5 at Phase Transition with Consideration of Its Range of Homogeneity. *Phys. Status Solidi A* **1976**, *37*, 541−546.

(35) Rúa, A.; Díaz, R. D.; Kumar, N.; Lysenko, S.; Fernández, F. E. Metal-Insulator Transition and Nonlinear Optical Response of Sputter-Deposited V_3O_5 Thin Films. *J. Appl. Phys.* **2017**, *121*, 235302.

(36) Osquiguil, E.; Maenhoudt, M.; Wuyts, B.; Bruynseraede, Y. Controlled Preparation of Oxygen Deficient $YBa_2Cu_3O_X$ Films. *Appl. Phys. Lett.* **1992**, *60*, 1627−1629.

(37) Hasen, J.; Lederman, D.; Schuller, I. K.; Kudinov, V.; Maenhoudt, M.; Bruynseraede, Y. Enhancement of Persistent Photoconductivity in Insulating High-T_C Thin Films. *Phys. Rev. B: Condens. Matter Mater. Phys.* **1995**, *51*, 1342−1345.

(38) Rampelberg, G.; De Schutter, B.; Devulder, W.; Martens, K.; Radu, I.; Detavernier, C. In Situ X-Ray Diffraction Study of the Controlled Oxidation and Reduction in the V−O System for the Synthesis of VO_2 and V_2O_3 Thin Films. *J. Mater. Chem. C* **2015**, *3*, 11357−11365.

(39) Choi, S.; Son, J.; Oh, J.; Lee, J.-H.; Jang, J. H.; Lee, S. Sharp Contrast in the Electrical and Optical Properties of Vanadium Wadsley (V_mO_{2m+1}, m> 1) Epitaxial Films Selectively Stabilized on (111)-Oriented Y-Stabilized ZrO_2. *Phys. Rev. Mater.* **2019**, *3*, 063401.

(40) Silversmit, G.; Depla, D.; Poelman, H.; Marin, G. B.; De Gryse, R. Determination of the V2p XPS Binding Energies for Different Vanadium Oxidation States (V^{5+} to V^{0+}). *J. Electron Spectrosc. Relat. Phenom.* **2004**, *135*, 167−175.

(41) Trastoy, J.; Kalcheim, Y.; del Valle, J.; Valmianski, I.; Schuller, I. K. Enhanced Metal−Insulator Transition in V_2O_3 by Thermal Quenching After Growth. *J. Mater. Sci.* **2018**, *53*, 9131−9137.

(42) Pennycook, S. J.; Zhou, H.; Chisholm, M. F.; Borisevich, A. Y.; Varela, M.; Gazquez, J.; Pennycook, T. J.; Narayan, J. Misfit

https://dx.doi.org/10.1021/acsami.0c18327
ACS Appl. Mater. Interfaces 2021, 13, 887−896

Accommodation in Oxide Thin Film Heterostructures. *Acta Mater.* **2013**, *61*, 2725−2733.
(43) Katzke, H.; Tolédano, P.; Depmeier, W. Theory of Morphotropic Transformations in Vanadium Oxides. *Phys. Rev. B: Condens. Matter Mater. Phys.* **2003**, *68*, 024109.
(44) Molaei, R.; Bayati, R.; Wu, F.; Narayan, J. A Microstructural Approach Toward the Effect of Thickness on Semiconductor-to-Metal Transition Characteristics of VO_2 Epilayers. *J. Appl. Phys.* **2014**, *115*, 164311.
(45) Narayan, J.; Bhosle, V. M. Phase Transition and Critical Issues in Structure-Property Correlations of Vanadium Oxide. *J. Appl. Phys.* **2006**, *100*, 103524.
(46) Brassard, D.; Fourmaux, S.; Jean-Jacques, M.; Kieffer, J. C.; El Khakani, M. A. Grain Size Effect on the Semiconductor-Metal Phase Transition Characteristics of Magnetron-Sputtered VO_2 Thin Films. *Appl. Phys. Lett.* **2005**, *87*, 051910.
(47) Zhang, S.; Kim, I. S.; Lauhon, L. J. Stoichiometry Engineering of Monoclinic to Rutile Phase Transition in Suspended Single Crystalline Vanadium Dioxide Nanobeams. *Nano Lett.* **2011**, *11*, 1443−1447.
(48) Zhang, Z.; Zuo, F.; Wan, C.; Dutta, A.; Kim, J.; Rensberg, J.; Nawrodt, R.; Park, H. H.; Larrabee, T. J.; Guan, X.; Zhou, Y.; Prokes, S. M.; Ronning, C.; Shalaev, V. M.; Boltasseva, A.; Kats, M. A.; Ramanathan, S. Evolution of Metallicity in Vanadium Dioxide by Creation of Oxygen Vacancies. *Phys. Rev. Appl.* **2017**, *7*, 034008.
(49) Sakai, J.; Limelette, P.; Funakubo, H. Transport Properties and c/a Ratio of V_2O_3 Thin Films Grown on C- and R-plane Sapphire Substrates by Pulsed Laser Deposition. *Appl. Phys. Lett.* **2015**, *107*, 241901.
(50) Brockman, J.; Samant, M. G.; Roche, K. P.; Parkin, S. S. P. Substrate-Induced Disorder in V_2O_3 Thin Films Grown on Annealed c-Plane Sapphire Substrates. *Appl. Phys. Lett.* **2012**, *101*, 051606.
(51) Andreev, V. N.; Klimov, V. A. Specific Features of Electrical Conductivity of V_3O_5 Single Crystals. *Phys. Solid State* **2011**, *53*, 2424−2430.
(52) *Powder Diffraction File 72-0977*; International Centre for Diffraction Data: PA, USA.
(53) Sidorov, V. A.; Waśkowska, A.; Badurski, D. V_3O_5 at High Pressure: A Possible Heavy Fermion 3d-Metal Oxide. *Solid State Commun.* **2003**, *125*, 359−363.
(54) Brockman, J.; Aetukuri, N. P.; Topuria, T.; Samant, M. G.; Roche, K. P.; Parkin, S. S. P. Increased Metal-Insulator Transition Temperatures in Epitaxial Thin Films of V_2O_3 Prepared in Reduced Oxygen Environments. *Appl. Phys. Lett.* **2011**, *98*, 152105.
(55) Shivashankar, S. A.; Honig, J. M. Metal—Antiferromagnetic-Insulator Transition in V_2O_3 Alloys. *Phys. Rev. B: Condens. Matter Mater. Phys.* **1983**, *28*, 5695−5701.
(56) Ueda, Y.; Kosuge, K.; Kachi, S. Phase Diagram and Some Physical Properties of V_2O_{3+x}. ($0 \leq x \leq 0.08$). *J. Solid State Chem.* **1980**, *31*, 171−188.
(57) Mendialdua, J.; Casanova, R.; Barbaux, Y. XPS Studies of V_2O_5, V_6O_{13}, VO_2 and V_2O_3. *J. Electron Spectrosc. Relat. Phenom.* **1995**, *71*, 249−261.
(58) Sawatzky, G. A.; Post, D. X-Ray Photoelectron and Auger Spectroscopy Study of Some Vanadium Oxides. *Phys. Rev. B* **1979**, *20*, 1546−1555.
(59) Demeter, M.; Neumann, M.; Reichelt, W. Mixed-Valence Vanadium Oxides Studied by XPS. *Surf. Sci.* **2000**, *454−456*, 41−44.

https://dx.doi.org/10.1021/acsami.0c18327
ACS Appl. Mater. Interfaces 2021, 13, 887−896